

# Numerical simulation of gas–liquid flow behavior in the nozzle exit region of an effervescent atomizer

Chunhua Sun<sup>1,2</sup> , Zhi Ning<sup>1</sup>, Xinqi Qiao<sup>2</sup>, Ming Lv<sup>1</sup>, Juan Fu<sup>1</sup>, Jin Zhao<sup>1</sup> and Xintao Wang<sup>1</sup>

## Abstract

The pressure drop and particular geometric structure of the nozzle exit region of an effervescent atomizer cause complex changes in the flow pattern, which could affect the spray performance. In this study, the gas–liquid two-phase flow behavior in the nozzle exit region of the effervescent atomizer was investigated numerically. The results show that the flow behaviors in the nozzle exit region have disparate characteristics with different upstream flow regimes. For upstream churn flow, the liquid film morphology is closely related to fluctuation in the gas–liquid velocity, and the flow parameters (fluids' velocities and gas void fraction) at the exit section vary regularly with time. For upstream bubbly flow, the instantaneous gas void fraction is determined by the bubble distribution inside the mixing chamber. The bubble will form a tadpole-like shape as a result of the complex flow field and the surface tension. The flow parameters at the exit section are in an oscillatory decay, and the fluctuation amplitude is larger than for churn flow. For upstream slug flow, the gas void fraction varies significantly with time. The discrete characteristic of the gas–liquid flow parameters at exit section is very obvious.

## Keywords

Bubbly flow, effervescent spray, flow regime, nozzle exit region, two-phase flow

Date received: 21 January 2018; accepted: 5 December 2018

## 1. Introduction

Effervescent atomization is a two-phase liquid atomization technique developed in the late 1980s by Lefebvre et al.,<sup>1–3</sup> and the promising technique for fields such as coating, fuel injection and combustion. This technique is differentiated from the premixing process of the two phases, and a variety of gas–liquid flow patterns are formed in the mixing chamber. This internal gas–liquid flow behavior plays an important role in the effervescent atomization.

The gas–liquid two-phase internal flow in effervescent atomizer has attracted increasing attention in the last 20 years. Several studies have demonstrated the close relationship between internal flow behavior and spray performance. Kim and Lee<sup>4</sup> qualitatively demonstrated the occurrence of different spray characteristics under varying flow regimes. Their researches revealed that the internal flow has a significant influence on the spray instability, and the slug flow was considered as the flow regime causing the most unstable spray. Lin et al.<sup>5</sup> experimentally investigated the internal

two-phase flows and the near-field structures of the corresponding sprays. The results indicated that the aerated-liquid spray is strongly related to the internal two-phase flow. Ramamurthi et al.<sup>6</sup> carried out experiments to investigate the spray under various flow regimes. Characteristics of the two-phase internal flow and spray performance over a wide range of gas–liquid mass ratios (GLRs), pressures and discharge orifice diameters were presented. Shepard<sup>7</sup> conducted research

<sup>1</sup>College of Mechanical and Electrical Engineering, Beijing Jiaotong University, Beijing, China

<sup>2</sup>Key Laboratory of Power Machinery and Engineering, Ministry of Education, Shanghai Jiao Tong University, Shanghai, China

### Corresponding authors:

Zhi Ning, College of Mechanical and Electrical Engineering, Beijing Jiaotong University, Beijing 100044, China.

Email: zhining@bjtu.edu.cn

Xinqi Qiao, Key Laboratory of Power Machinery and Engineering, Ministry of Education, Shanghai Jiao Tong University, Shanghai 200240, China.

Email: qiaoxinqi@sjtu.edu.cn



to explore the effect of bubble size on spray performance. The results revealed that the bubble size has a significant influence on the spray droplet size and spray unsteadiness. To some extent, the internal flow plays a decisive role in effervescent atomization. An understanding of the internal flow behavior enables the control of internal flow pattern, which is the basis for achieving good atomization.

Both experimental and theoretical methods have been used to strengthen the understanding of internal flow pattern and its evolution. Rahman<sup>8</sup> developed a visualization experiment system to observe the internal flow. Bubble size and slug frequency were measured, and the linear relationship between the bubble size and gas-to-liquid mass ratio was also obtained. Esfarjani and Dolatabadi<sup>9</sup> performed a three-dimensional simulation of the internal flow in an effervescent atomizer. The results indicated that at low GLRs, an increase in the aeration level has a significant effect on the liquid film thickness.

Previous studies of the internal flow found that the internal flow pattern changes greatly in the nozzle exit region. Catlin and Swithenbank<sup>10</sup> captured images of a bubble approaching the nozzle exit, and a large deformation of the bubble was obtained. Lörcher et al.<sup>11</sup> further investigated the bubble deformation in the nozzle exit region. The results showed that the bubble in the nozzle exit region would be stretched by the pressure drop and deformed into smaller bubbles. Ramamurthi et al.<sup>6</sup> carried out a two-dimensional simulation to study the features of internal flow and spray. The results showed that the initial spherical bubble would be elongated in the nozzle exit region. Li et al.<sup>12</sup> investigated and described the influence of internal geometries and liquid physical properties on the two-phase flow structure in the final discharge orifice. It was found that the sizes of bubble and the liquid film were significantly affected by the atomizer geometries and liquid properties.

The nozzle exit region of the effervescent atomizer connects the internal gas–liquid mixing chamber and the external environment. The size of nozzle exit region is much smaller than mixing chamber, which accelerates the two-phase flow since the fluids flowing into the nozzle exit region from the mixing chamber. In addition, the pressure drop in the nozzle exit region increases the gas–liquid flow velocity. These combined effects on the gas–liquid two-phase cause complex changes on the two-phase flow pattern. Significant changes in the gas–liquid two-phase flow structure in the nozzle exit region have been observed in previous research. However, few studies have examined the effect of varying upstream flow regimes on the evolution of two-phase flow structures. It is also rare to find quantitative studies on gas–liquid two-phase flow behaviors

in the exit region, such as liquid film pulsation in churn flow, parameters' of bubble group in bubbly flow, and gas void fraction in slug flow.

The understanding of gas–liquid flow behavior inside the nozzle exit region is the bridge linking internal flow and external flow. Investigation of the gas–liquid two-phase flow behavior in the nozzle exit region could reveal the spray characteristics especially the features of jet instability. Owing to the complex phase structure, it is difficult to investigate the morphological evolution of different flow regimes by experimental visualization methods. In this study, numerical simulation method was used to study the gas–liquid two-phase flow in the exit region of an effervescent atomizer. The simulation model was established based on the volume of fluid (VOF) method using the commercially available computational fluid dynamics software ANSYS FLUENT 14.0. The evolution and development of the gas–liquid two-phase flow for various upstream flow regimes were investigated. Morphological changes in bubbles passing through the nozzle exit region were also analyzed. Finally, characteristics of gas–liquid flow parameters at the nozzle exit section were investigated.

## 2. Methodology

### 2.1. Geometric model

The geometric model of the exit region of an effervescent atomizer used in the present study is shown in Figure 1. To consider the effects of different flow regimes, the computational domain is extended to include the partial mixing chamber.

The diameter and length of the mixing chamber are 6 mm and 8 mm, respectively. The diameter and length of the exit orifice are 1.2 mm and 2.4 mm, respectively.

### 2.2. Governing equations

In the present study, the VOF method was used to track the location of the phase interface. The fluid volume fraction function,  $\alpha$ , is expressed as follows<sup>13</sup>

$$\alpha(x, t) = \begin{cases} 1, & \text{gas - phase} \\ 0 < \alpha < 1, & \text{gas - liquid two - phase} \\ 0, & \text{liquid - phase} \end{cases} \quad (1)$$

When using the VOF method, interface reconstruction and advancing of the interface with time are two important problems. The piecewise-linear interface calculation (PLIC) method was used to reconstruct the gas–liquid interface, and an operator non-splitting algorithm was employed to advance the interface with time.

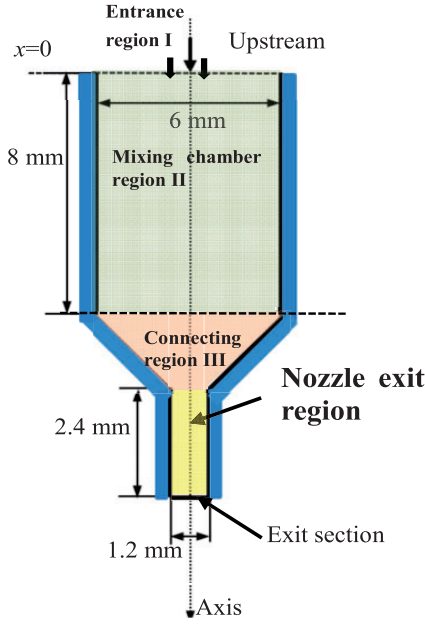


**Figure 1.** Schematic of the geometric model of the nozzle exit region.

In this study, the governing equations for the fluid flows could be expressed as

$$\frac{\partial \rho}{\partial t} + \nabla \cdot \rho \mathbf{V} = 0 \quad (2)$$

$$\frac{\partial \rho \mathbf{V}}{\partial t} + \nabla \cdot \rho \mathbf{V} \mathbf{V} = \nabla \cdot \boldsymbol{\tau} - \nabla p + \rho \mathbf{g} + \sigma w \mathbf{n} \quad (3)$$

where  $\rho$  is the fluid density;  $\mathbf{V}$  is the fluid velocity,  $p$  is the fluid pressure;  $\mathbf{g}$  is the gravitational acceleration which is  $9.8 \text{ kg}\cdot\text{m/s}^2$ . The last item ( $\sigma w \mathbf{n}$ ) considers the surface tension force which is solved by the continuum surface tension (CSF model<sup>14</sup>) method;  $\sigma$  is the surface tension coefficient;  $w = \nabla \cdot (\mathbf{n}/|\mathbf{n}|)$ , is the curvature at the interface;  $\mathbf{n}$  is the gradient vector of volume fraction;  $\boldsymbol{\tau}$  is the turbulent (Reynolds) stress, which is calculated according to the Boussinesq approximation, and can be expressed as

$$\boldsymbol{\tau} = \mu^t ((\nabla \mathbf{V} + \nabla \mathbf{V}^T) - \frac{2}{3} \mathbf{I} \nabla \cdot \mathbf{V}) - \frac{2}{3} \rho k \mathbf{I} \quad (4)$$

where  $\mu^t$  is the turbulent viscosity,  $k$  is the turbulence kinetic energy, and  $\mathbf{I}$  is the unit tensor.

Considering the high flow velocity in the nozzle exit region, the turbulence should also be taken into account. A standard  $k$ - $\varepsilon$  turbulence model was used to describe the turbulence. The standard  $k$ - $\varepsilon$  turbulence model consists of the turbulent kinetic energy,  $k$ , and

the transport equation for the turbulent energy dissipation rate,  $\varepsilon$ , which are expressed as follows<sup>15</sup>

$$\frac{\partial}{\partial t}(\rho k) + \nabla \cdot (\rho k \mathbf{V}) = \nabla \cdot \frac{\mu^d}{\sigma_k} \nabla k + G - \rho \varepsilon \quad (5)$$

$$\frac{\partial}{\partial t}(\rho \varepsilon) + \nabla \cdot (\rho \varepsilon \mathbf{V}) = \nabla \cdot \frac{\mu^d}{\sigma_\varepsilon} \nabla \varepsilon + \frac{\varepsilon}{k} (C_1 G - C_2 \rho \varepsilon) \quad (6)$$

where  $G$  is the average turbulent kinetic energy caused by the velocity gradient as expressed in equation (7);  $\mu^d$  is the dynamic viscosity;  $\sigma_k$  and  $\sigma_\varepsilon$  are the Prandtl number of the turbulent kinetic energy and the turbulent energy dissipation rate, respectively; and  $C_1$  and  $C_2$  are constants. The constants in this formula referring to the experimental results of Launder and Spalding<sup>15</sup> are assigned as follows:  $C_1 = 1.44$ ,  $C_2 = 1.92$ ,  $\sigma_k = 1$ , and  $\sigma_\varepsilon = 1.3$ .

$$G = \sum_i (\boldsymbol{\tau} \cdot \nabla \mathbf{V}) \quad (7)$$

where the subscripts  $i = 1$  and  $2$  represents the gas and liquid phase, respectively.

Knowing values of  $k$  and  $\varepsilon$  for each phase, the turbulent viscosities used in equation (5) can be calculated in the usual way

$$\mu^t = C_\mu \rho \frac{k^2}{\varepsilon} \quad (8)$$

where  $C_\mu = 0.09$  is the coefficient from the standard  $k$ - $\varepsilon$  model.

The fluid density  $\rho$ , and dynamic viscosity  $\mu^d$  are depend on the VOF fraction function,  $\alpha$ , and can be expressed as

$$\rho = \alpha_1 \rho_1 + \alpha_2 \rho_2 \quad (9)$$

$$\mu^d = \alpha_1 \mu_1^d + \alpha_2 \mu_2^d \quad (10)$$

$$\alpha_1 + \alpha_2 = 1 \quad (11)$$

The gas–liquid interface can be transported using the following “VOF equation”

$$\frac{\partial \alpha}{\partial t} + (\mathbf{V} \cdot \nabla) \alpha = 0 \quad (12)$$

An ideal gas relationship connects the density with the pressure for the gaseous phase. To consider the compressibility of the gas phase, the gas state equation and energy equation are introduced as follows

$$\rho_1 = \frac{p}{\frac{R}{M_w} T} \quad (13)$$

$$\frac{\partial}{\partial t}(\rho E) + \nabla \cdot (\mathbf{v} (\rho E + p)) = \nabla \cdot (k_{\text{eff}} \nabla T) \quad (14)$$

where  $R$  is the universal gas constant,  $Mw$  is the molecular weight, and  $k_{eff}$  is the thermal conductivity. In the VOF model, the energy,  $E$ , and temperature,  $T$ , are calculated as follows

$$E = \frac{\alpha_1 \rho_1 E_1 + \alpha_2 \rho_2 E_2}{\alpha_1 \rho_1 + \alpha_2 \rho_2} \quad (15)$$

$$T = \frac{\alpha_1 \rho_1 T_1 + \alpha_2 \rho_2 T_2}{\alpha_1 \rho_1 + \alpha_2 \rho_2} \quad (16)$$

### 2.3. Solvability conditions and verification

Water and air were used as the computational liquid and gas in the numerical simulations. The initial and boundary conditions were defined according to previously published models.<sup>16–18</sup> The upstream flow regime and initial flow morphology parameters such as the liquid film and bubble size were determined through the visualization experiments.<sup>19</sup> The atomizer geometries (mixing chamber

diameter, exit orifice diameter, exit orifice length) are same with the visualization experiments, as can be seen in Figure 2 (left). The diameter of upstream entrance region is same with the mixing chamber diameter. The detailed operating conditions for investigated case are shown in Table 1, and the upstream flow regime of cases 1,2,6,8 in the flow regime map is shown in Figure 2 (right).

The horizontal and vertical coordinates of the flow regime map in the experiments are superficial liquid and gas velocities,<sup>20</sup> and are defined as follows

$$\text{Superficial gas velocity: } v_{sg} = \frac{4Q_g}{\pi d_n^2} \quad (17)$$

$$\text{Superficial liquid velocity: } v_{sl} = \frac{4Q_l}{\pi d_n^2} \quad (18)$$

where  $Q_g$  and  $Q_l$  are the gas and liquid volume flow rates, respectively;  $d_n$  is the diameter of the mixing chamber which is 6 mm.

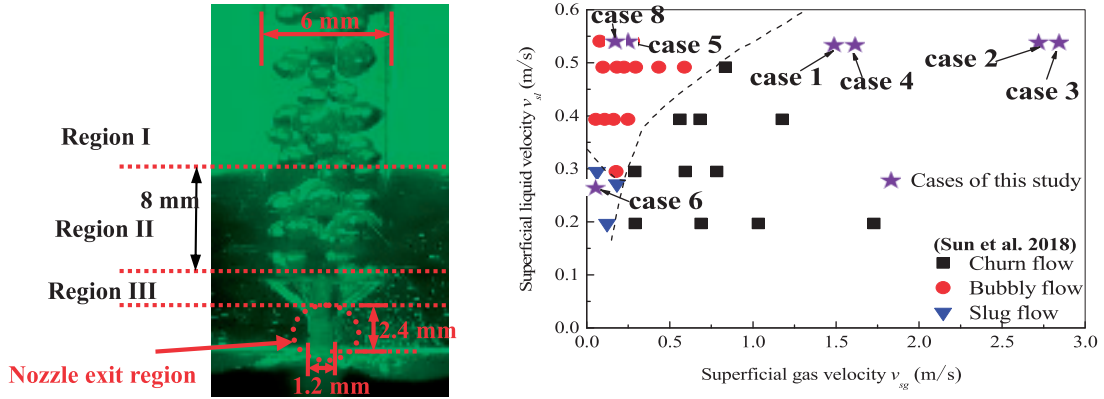


**Figure 2.** The upstream flow regimes of cases in the flow regime map (Right) by previous experiments<sup>19</sup> with the same geometries (Left).

**Table 1.** Flow rates and flow regimes for investigated cases.

Case	Related figure	Flow regime	Liquid mass flow rate $\dot{m}_l$ (g/s)	Gas-to-liquid mass ratio GLR (%)	Supplementary condition
1	Figures 10(a) and 25	Churn flow	16	1.2	—
2	Figure 10(b)	Churn flow	16	2.3	—
3	Figure 11(a)	Churn flow	16	1.48	$w_{s0} = 0.35$ mm
4	Figure 11(b)	Churn flow	16	0.72	$w_{s0} = 0.60$ mm
5	Figures 13 to 15	Bubbly flow	16	0.082	Bubble group, initial bubble diameter is 1 mm
6	Figures 16, 17 and 27	Slug flow	8	0.05	Equivalent diameter of slug is about 3.5 mm
7	Figures 18 to 24	Bubbly flow	16	—	Single bubble, initial bubble diameter is 1 mm
8	Figure 26	Bubbly flow	16	0.07	—

The upstream flow entrance was of gas–liquid two-phase velocity inlet boundary, and the specific value depended on the operating conditions. The nozzle exit section was of the pressure outlet boundary, and has a value of  $1 \times 10^5$  Pa (static pressure). The wall was of a no-slip wall boundary. The Green Gauss node based method and the pressure-implicit with splitting of operators (PISO) scheme were used to calculate the gradient of pressure, velocity components, volume fraction, and the pressure-velocity coupling. The second order up

wind scheme was used to solve both the momentum and energy equations.

To verify the correctness of the proposed numerical model, a qualitative case (a single bubble passing through the nozzle exit region) and quantitative results (velocities at nozzle exit of varied gas–liquid mass ratios (GLRs)) were simulated.

The numerical result of qualitative case was then compared to results of the visualization experiments conducted by Lörcher et al.<sup>11</sup> The atomizer geometry is shown in Figure 3. The inlet pressure of the nozzle exit region is  $6 \times 10^5$  Pa, and the outlet pressure is  $1 \times 10^5$  Pa. The initial diameter of the bubble entering the exit region from the mixing chamber is approximately 1.2 mm.

The simulation is conducted with the same geometric parameters and operating parameters as the experiments.<sup>11</sup> Figure 4 shows the comparison of the numerical results and the published experimental results.

The comparison shown in Figure 4 verifies that the simulation model proposed in this study could accurately predict the shape change in bubbles in the nozzle exit region.

The numerical results of quantitative cases were compared to results of the experimental measurements of Liang.<sup>21</sup> The atomizer geometry and solvability conditions were kept same with Liang's experiments, as can be seen in Figure 5 and Table 2. The velocity field (velocity along the axis direction of atomizer) was numerically calculated, as can be seen in Figures 6 and 7.

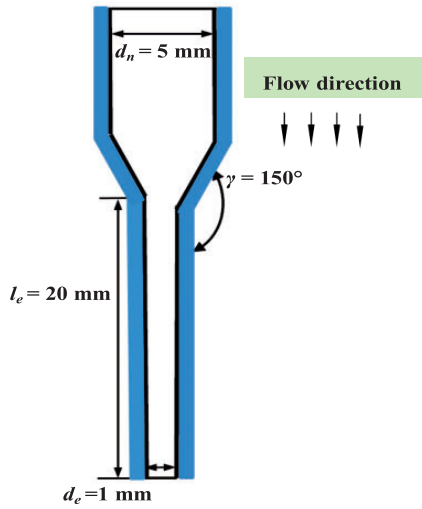


**Figure 3.** Schematic of the atomizer in experiments conducted by Lörcher et al.<sup>11</sup>

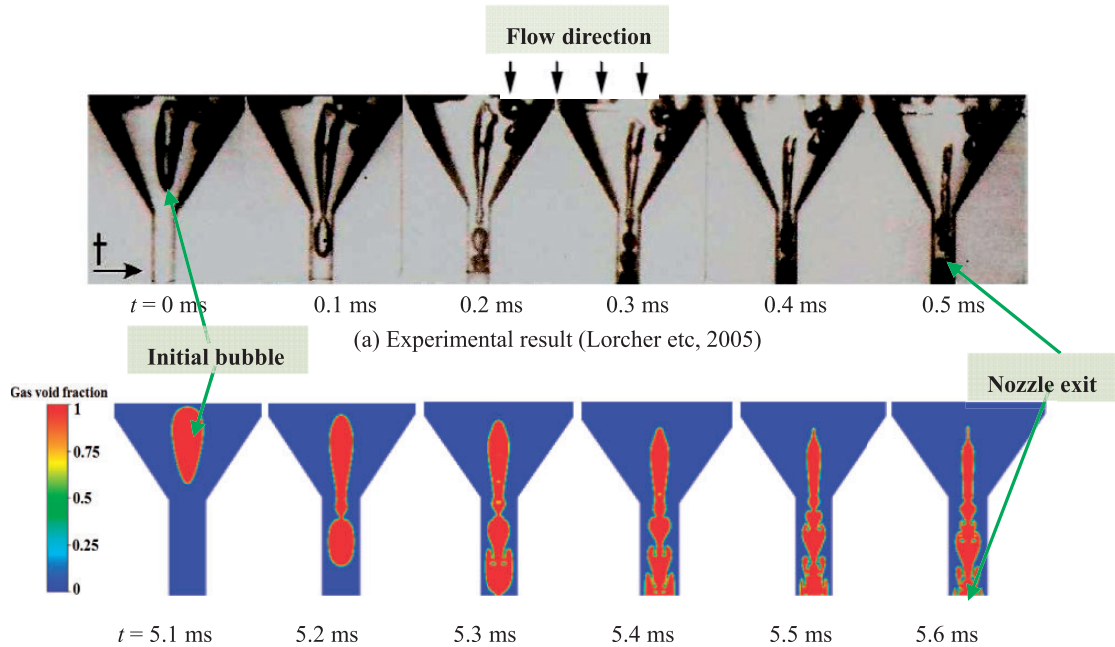


**Figure 4.** Comparison of numerical and experimental results. (a) Experimental result.<sup>11</sup> (b) Numerical result.



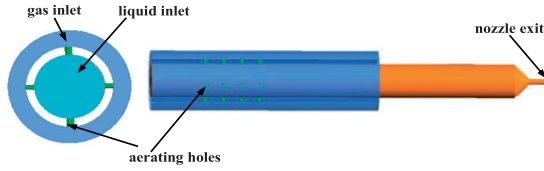


Figure 5. Geometric model of quantitative verifying case.

Table 2. Solvability conditions and experiments results of verifying case.

Liquid mass flow rate (kg/h)	Gas-liquid mass ratio GLR (%)	Velocity at nozzle exit from experiment (m/s) <sup>21</sup>	Reynolds number
300	3.8	46.7	30965
420	5.7	141.1	58394
480	7.0	198.1	78495

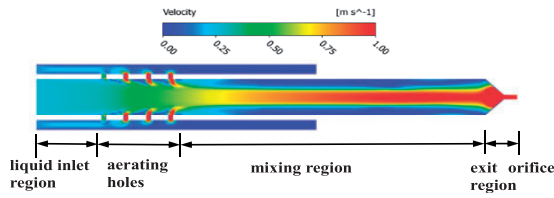


Figure 6. The velocity field of inside the effervescent atomizer.

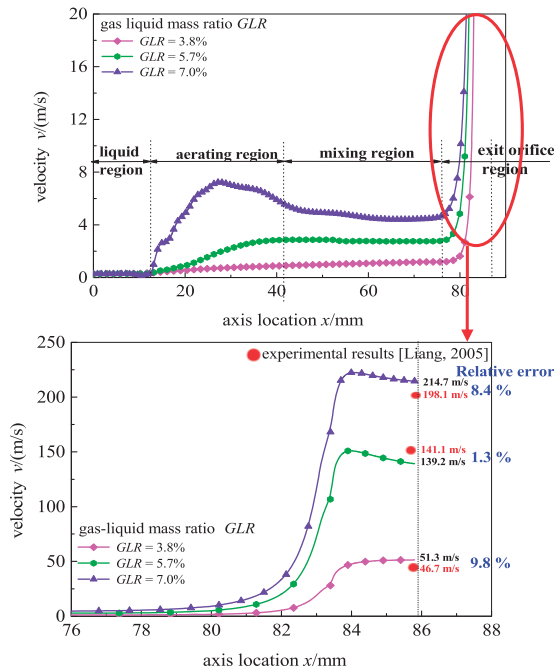


Figure 7. The velocities of different GLRs along the axis.

The comparison in Figure 7 shows that the relative error of velocities between numerical and experimental results is below 10%. It indicates that the simulation model could predict the velocity in the nozzle exit region. In addition to refining mesh, a modified turbulence model detailed considering the mutation of sound velocity and coupling the instantaneous gas void fraction at the nozzle exit is necessary for further improving the simulating accuracy.

In this paper, the velocity at the nozzle exit was used as a parameter to verify the independence of the grid. In the mesh independence analysis, the liquid mass flow rate is 16 g/s and the gas-liquid mass ratio is 1.6%. The average velocity at the nozzle exit calculated by different grid numbers is shown in Figure 8.

It can be seen in Figure 8 that the velocity at nozzle exit tends to be stable since the grid number increasing from 70,000 to more than 1000,000. Considering the resolution of the flow field structure and the calculation cost, the grid number of the computational model was finally controlled at about 400,000. The grid resolution was determined according to the geometric size and velocity gradient. The gas-liquid inlet diameter was 6 mm, and was discretized with 250 grid points; this yielded a grid cell size of  $2.4 \times 10^{-5}$  m. Meanwhile, the grid was densified in the nozzle exit, and the grid cell size was  $5 \times 10^{-6}$  m. Depending on the grid resolution and local velocity, a time step varying between  $2 \times 10^{-7}$  and  $1 \times 10^{-6}$  s was used in the simulations.

In the present study, the flow regime transition was not investigated. The flow regime transition is very sensitive to the initial condition and disturbance. However, in the present established model, the initialization of flow field is simply processed, and the turbulent intensities at the inlet and outlet are fixed values without considering the time-varied gas void fraction. Therefore, the limitation of the model is that it could not simulate the flow regime transition and predict the boundary of flow regime.

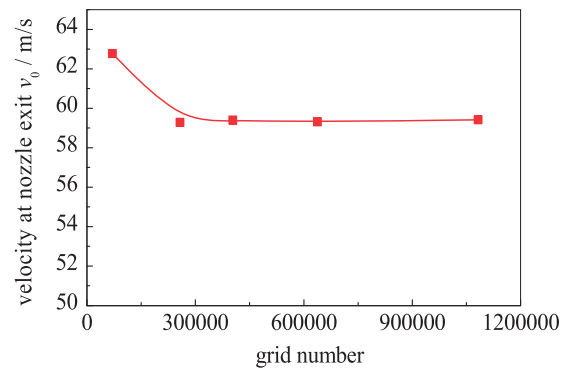


Figure 8. The results of the grid verification diagram for gas-liquid flow model in mixing chamber.

### 3. Results and discussion

#### 3.1. Flow behavior under different flow regimes

In the effervescent atomizer, the flow field and development of the gas–liquid form in the mixing chamber is stable. However, in the nozzle exit region, as a result of the significant change in structure and sudden pressure drop, the gas–liquid two-phase flow patterns changes dramatically with time and space. The different gas–liquid two-phase flow patterns inside the exit region will show completely different characteristics. In this section, the evolution of gas–liquid flow shape and development of gas–liquid two-phase flow in the nozzle exit region are studied to reveal the gas–liquid characteristics of different upstream flow regimes.

There are three typical flow regimes (slug, bubbly, or churn flow) in the effervescent atomizer determined by bubble generation and bubble dynamics, as shown in Figure 9 which was observed by the previous experiment,<sup>19</sup> and the gas–liquid structures of the three flow regimes could be well described by Hewitt and Hall Taylor<sup>22</sup>: In slug flow, some of the gas bubbles have nearly the same cross-section as that of the channel and move along in the characteristic bullet-shaped bubbles as illustrated in Figure 9(a). The bubbles of gas are separated by lengths occupied mainly by liquid which may or may not contain a dispersion of smaller gas bubbles.<sup>22,23</sup> In churn flow, there is a liquid layer or film on the chamber walls which presents a continuous interface to a stream consisting mainly of gas, which flows in the center of the channel, as can be seen in Figure 9(b). Bubbly flow is the most general flow regime in effervescent atomizer, and the gas phase is

distributed in discrete bubbles within a liquid continuum, as can be seen in Figure 9(c).

The churn flow is common in the effervescent atomizer, and the liquid film is an important gas–liquid shape characteristic. In churn flow, the gas–liquid interface is easily altered by the sudden change of atomizer geometry and the pressure drop in the nozzle exit region.

The variation in gas–liquid flow film with time in the nozzle exit region is shown in Figure 10. The results are obtained at the same liquid mass flow rate (16 g/s), but different gas-to-liquid mass ratios (GLR of 1.2% and 2.3%).

As shown in Figure 10(a), the flow inside the nozzle is basically stable in the mixing chamber when the gas–liquid mass ratio is small (GLR = 1.2%). However, the gas–liquid shape in the nozzle exit region changes significantly with time. In the nozzle exit region, the gas–liquid shape is strongly affected by the nozzle structure and pressure boundary, and the interface between the gas and liquid is quite complex, making it difficult for the liquid film forming.

The gas–liquid flow pattern evolves into a more stable flow at high GLR condition (GLR = 2.3%), as shown in Figure 10(b). It shows that the liquid film in the mixing chamber distant from the nozzle exit region is relatively stable, and the liquid film has not yet disappeared in the exit region. However, the liquid film is still in a fluctuating state.

In churn flow, the gas core greatly stretches, expands, and accelerates under the effect of pressure exit. Furthermore, the turbulence effect on the stretched structures brings about the structural fluctuation.

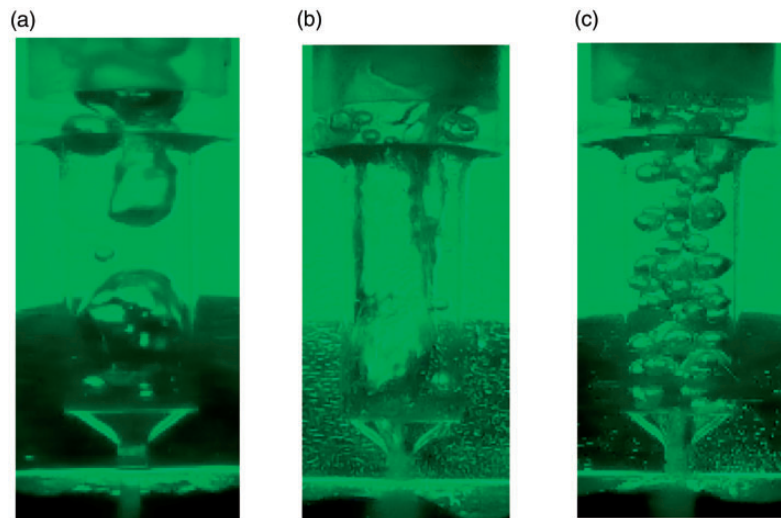


**Figure 9.** Gas–liquid flow regimes inside the mixing chamber.<sup>19</sup> (a) Slug flow (b) Churn flow (c) Bubbly flow.

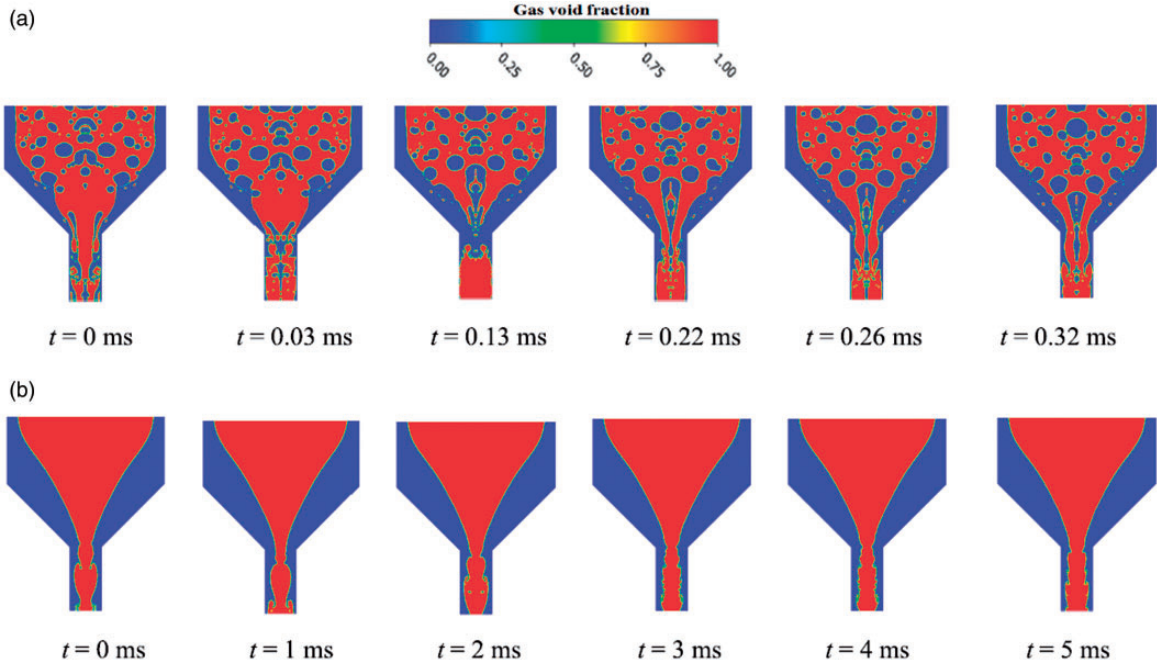


**Figure 10.** Liquid film shape of churn flow in the nozzle exit region. (a) GLR = 1.2% (case 1). (b) GLR = 2.3% (case 2).

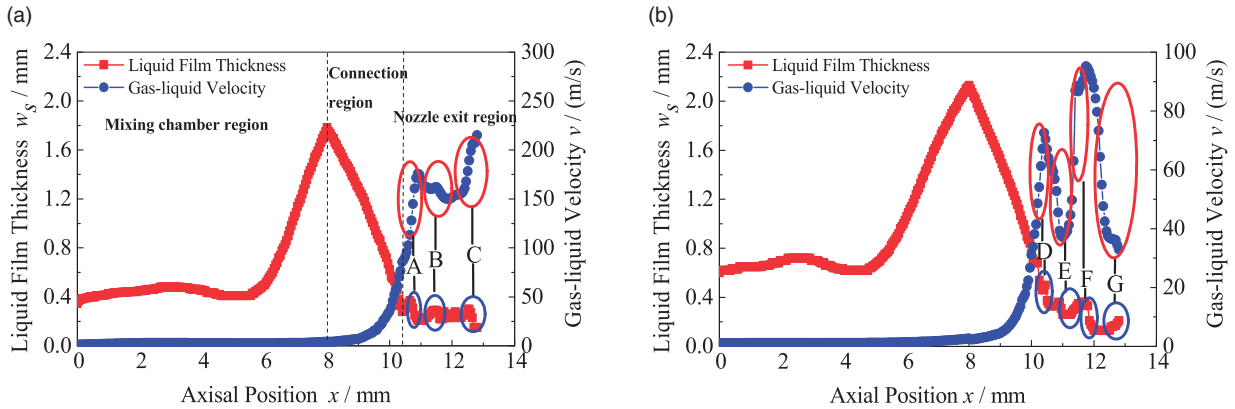


**Figure 11.** Liquid film thickness and velocity of churn flow at the exit orifice along the center axis. (a)  $w_{s0} = 0.35$  mm (case 3, GLR = 1.48%) (b)  $w_{s0} = 0.6$  mm (case 4, GLR = 0.74%).

The stretched structure and turbulent intensity are sensitive to each other. Indeed, the turbulence intensity in the calculating domain especially at the nozzle exit varies with time. While, ANSYS Fluent requires specification of transported turbulent quantities (turbulent kinetic energy and turbulent dissipation rate at the nozzle exit), and this limitation somehow reduces the predicting accuracy of the size and strength of the stretched structures.

Figure 11 shows the variations of the liquid film thickness and the gas-liquid velocity along the axial direction. The liquid mass flow rates of Figure 11(a)

and (b) are of same (16 g/s), and the difference is the initial liquid film thickness  $w_{s0}$ .

As can be seen from Figure 11, despite the initial difference in liquid film thickness, the variation law of liquid film thickness along the axial direction in the nozzle exit region is similar. In the early part of mixing chamber, the film thickness and velocity along the axial are relatively stable. Owing to the structural change of the connection region, the liquid film thickness rises first and then decreases quickly. In the nozzle exit region, the sudden pressure drop causes rapid gas expansion, and sharply expanding gas could extrude



the liquid film to make it thinner and accelerate both gas and liquid velocities. In addition, both liquid film thickness and gas–liquid velocity in the exit orifice fluctuate obviously.

The results shown in Figure 11 also quantitatively demonstrate the close relationship between fluctuation of the liquid film thickness and the gas–liquid velocity by comparing the characteristic peaks and valleys (marked as A–G in Figure 11) in the nozzle exit region. The change in liquid film thickness is approximately simultaneously changed with gas–liquid velocity. The gas velocity increases, the liquid film thickness decreases, as shown in Figure 11(a) and (b). The liquid film thickness is the smallest at the highest gas–liquid velocity.

In bubbly flow, the bubble experiences a morphological stretching in the nozzle exit region. Investigation of the morphology of bubbles in bubbly flow will help deepen the understanding of the motion and variation of bubbles in the exit region.

A bubbly flow regime is established in the mixing chamber to investigate the morphological evolution of a bubble group flowing through the nozzle, as shown in Figure 12.

Figure 13 shows the time-varied morphological of the bubble group during the bubble group passing

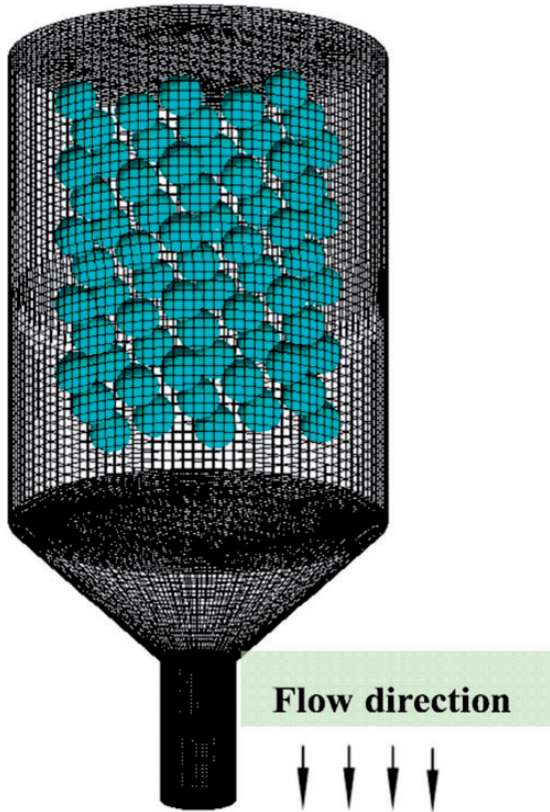


**Figure 12.** Bubble group in the mixture chamber.

through the nozzle exit region. The liquid mass flow rate is 16 g/s, and the initial bubble diameter is 1 mm.

As shown in Figure 13, the bubble shapes change dramatically as the bubble group enters the nozzle contraction structure ( $t > 0.25$  s). Due to the effect of the large pressure gradient, the bubbles stretch and coalesce in the nozzle exit region. The bubble distribution and bubble coalescence take effects on the bubble quantity and bubble shape inside the nozzle exit region. As Figure 13 shows, there may be one or more bubbles passing through the nozzle exit region at the same time. It should be noted that, in the nozzle exit region, the differences of bubble number, gas volume, and bubble shape have direct impacts on the instantaneous local gas void fraction, and further affects the jet stability which has been observed by Shepard.<sup>7</sup> In a sense, a homogeneous bubbly flow the mixing chamber is the key to achieve a stable jet.

The simulation results in Figure 13 show that there are multiple bubbles flowing into the nozzle exit region at same time, and these bubbles will be stretched, twisted together, and polymerized in the nozzle exit region.

Figure 14 shows the experimental and numerical results for the morphologies of multiple bubbles in the nozzle exit region. Both experimental and numerical results indicate that the stretched bubbles will become entangled, and the multiple spherical bubbles will then form a large “filamentous bubble” surrounded by liquid. The new gas–liquid two-phase flow structure is more similar to an annular flow.

Figure 15 shows the variation in volume and surface area of the bubble group passing through the nozzle exit region. The volume and surface area of the bubble group in the plot are dimensionless parameters derived by dividing by the initial bubble group volume and surface area, respectively.

Dimensionless bubble group volume:

$$\lambda_V = \frac{V_{\text{bubble group}}(t > 0)}{V_{\text{bubble group}}(t = 0)} \quad (19)$$

Dimensionless bubble group surface:

$$\lambda_S = \frac{S_{\text{bubble group}}(t > 0)}{S_{\text{bubble group}}(t = 0)} \quad (20)$$

where  $V_{\text{bubble group}}$  and  $S_{\text{bubble group}}$  are the volume and surface area of bubble group, respectively.

As shown in Figure 15, the bubble group volume increases as the bubble group moves to the nozzle exit region (0–0.3 s) due to gas expansion caused by the pressure drop. However, comparing to the effect of gas expansion on the increase of bubble group surface area, the bubble coalescence has a more influence on decreasing the surface area, and the bubble group

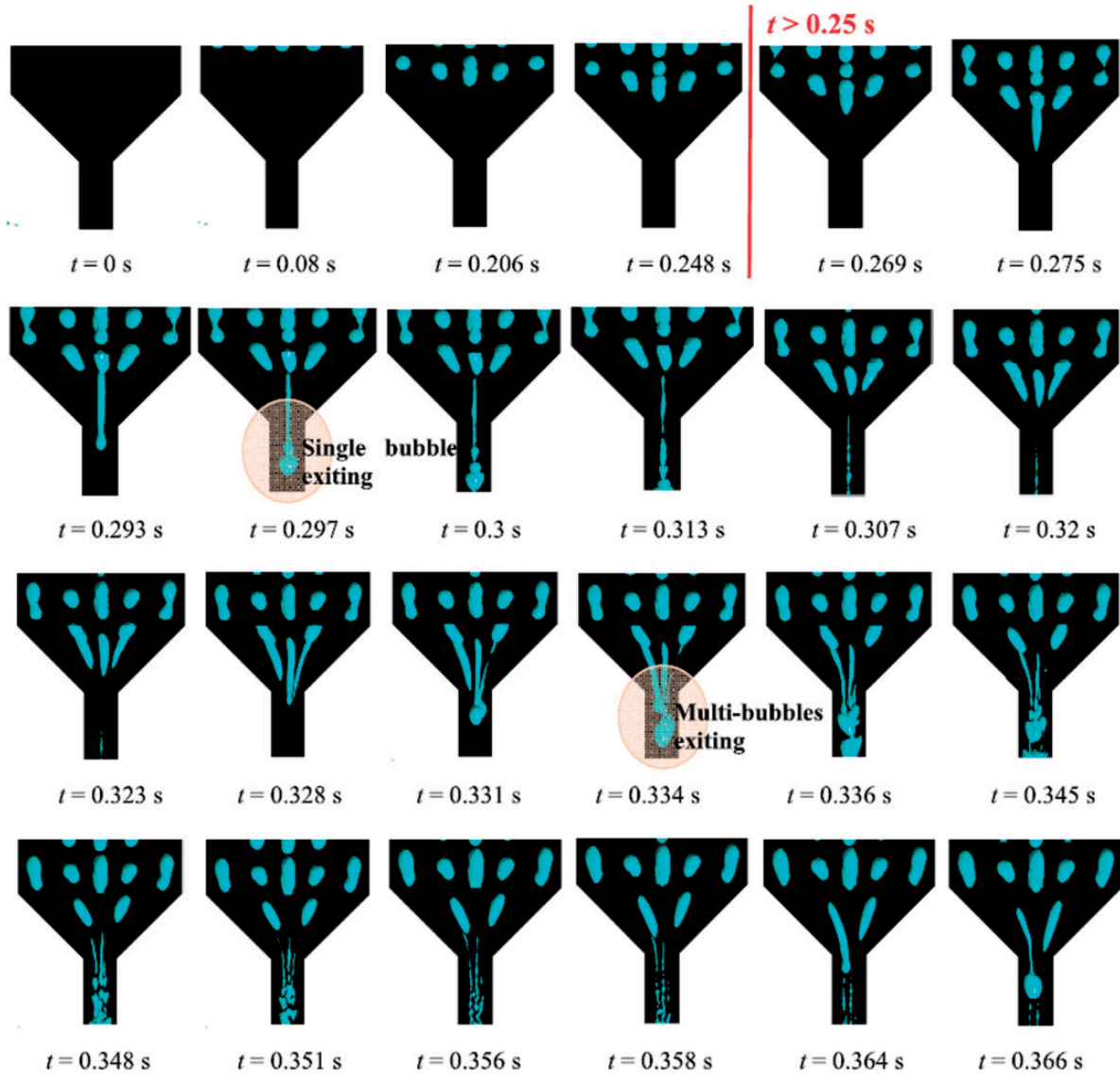


**Figure 13.** Shape changes in a bubble group passing through the nozzle exit region (case 5).

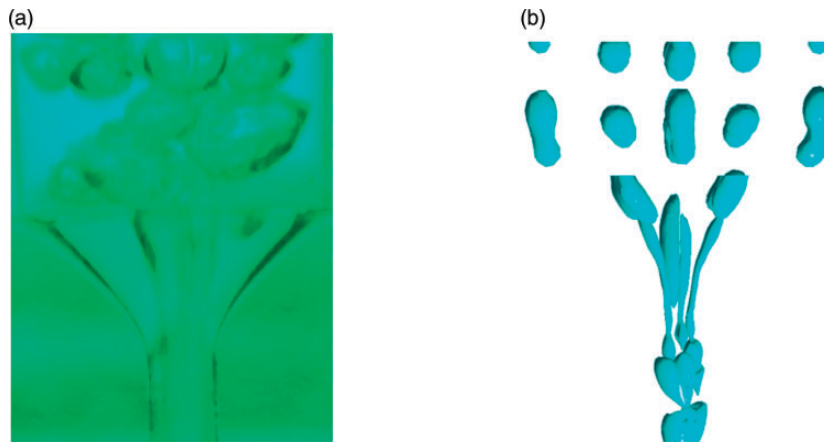


**Figure 14.** Stretching phenomena for multiple bubbles entering the nozzle exit region. (a) Experimental result.<sup>19</sup> (b) Numerical result (case 5,  $t = 0.336$  s).

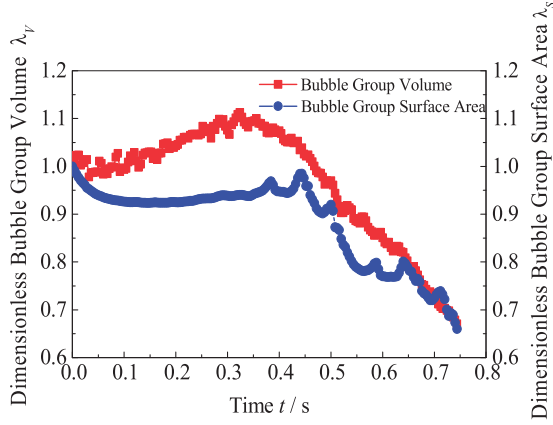


**Figure 15.** Variation in shape parameters of the bubble group (case 5).

surface area will slowly decrease as the bubble group moves to the nozzle exit region (0–0.3 s). As the bubble group flows away from the nozzle exit region ( $t > 0.3$  s), both bubble group volume and surface area decrease over time.

Slug flow, large bubbles of gas are separated by lengths occupied mainly by liquid which may or may not contain a dispersion of smaller gas bubbles.<sup>22</sup> For upstream slug flow, jet discontinuity is more common compared to churn and bubbly flow.<sup>24</sup> Analysis of the development of slug flow inside the nozzle exit region is of great importance for understanding jet discontinuity in effervescent atomization.

Figure 16 shows the gas morphology flowing through the nozzle exit region with an upstream slug flow. The results indicate that the gas distribution of

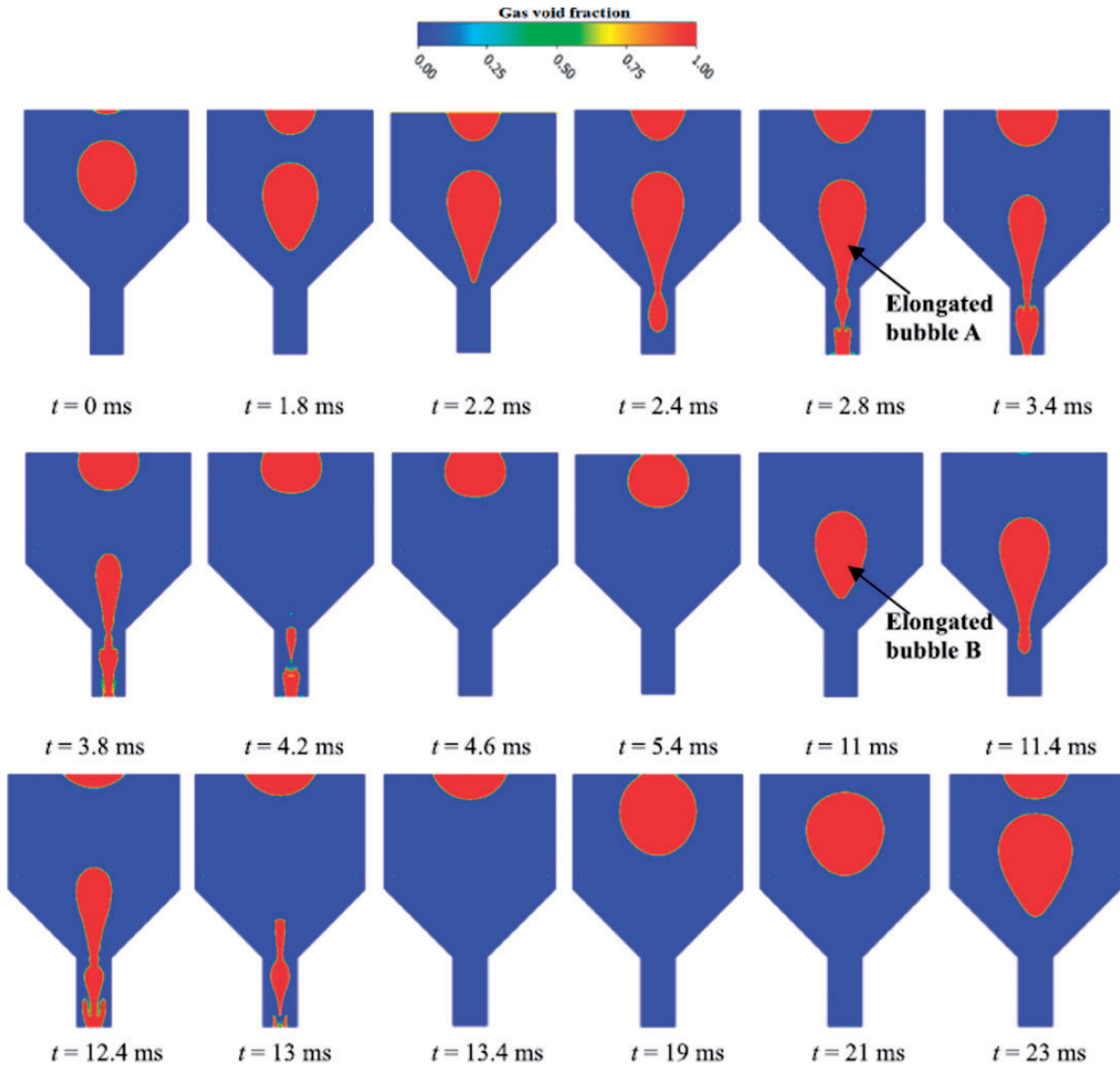


**Figure 16.** Shapes of gas passing through the exit orifice in a slug flow (case 6).

slug flow in the nozzle exit region exhibits obvious intermittent feature.

The morphological evolution of an elongated gas bubble flowing through the nozzle exit region includes deformation, stretching, and expansion processes, which are similar to those for a single bubble in bubbly flow. Large bubbles (e.g. A, B) could also be broken into several small bubbles.

Figure 17 shows the mean of gas void fraction over the nozzle exit region with time during the slug flowing through the nozzle exit region.

Figure 17 shows that the mean gas void fraction of the nozzle exit region is significantly discrete with time. The gas void fraction increases as the large bubbles (e.g. A and B) entering the nozzle exit region and expanding due to the pressure drop. Although the stretching of large bubble benefits for a uniform distribution of the gas phase, while a single liquid phase exiting the nozzle

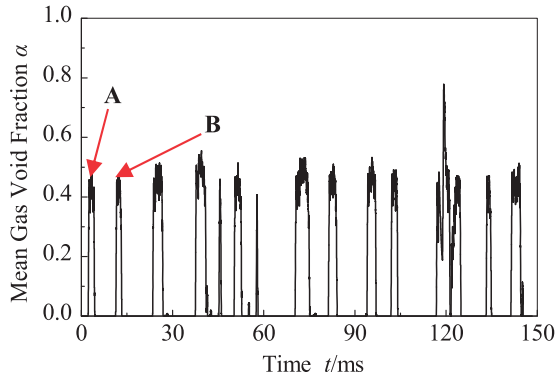


**Figure 17.** Variation in mean gas void fraction with time in the nozzle exit region (case 6).

exit region is still a recurrent phenomenon owing to the large intervals between gas bubbles reaching the exit orifice.

### 3.2. Morphological change in single bubble

Bubbly flow is a common and ideal gas–liquid internal flow pattern in an effervescent atomizer. Bubble morphology is greatly affected by changes of flow field in the nozzle exit region.<sup>25–27</sup> For bubbly flow, it is difficult to conduct a detailed analysis of bubble morphological changes owing to the disturbance of multiple bubbles intertwining. The morphological characteristics of a bubble group are closely related to the ones of a single bubble. Therefore, examination of a single bubble could contribute to understanding of the morphological evolution of bubbly flow in the nozzle exit region.

Figure 18 shows the morphological change of a single bubble moving through the nozzle exit region. The liquid mass flow rate is 16 g/s, and the initial diameter of a bubble is 1 mm.

As Figure 18 shows, the bubble morphology changes little before entering the exit orifice ( $t < 3.8$  ms). The bubble begins to elongate as it moves into the contraction structure between the mixing chamber and nozzle exit region ( $t > 5$  ms). After the bubble entering the nozzle exit region, the effect of the pressure drop causes the front part of the bubble to expand, and gradually the bubble forms a tadpole-like shape with a large head and long tail. Moreover, partial tensile fracture is likely to occur under the stretching action induced by the large pressure gradient. Because the gas phase is most concentrated in the front of the bubble, gas

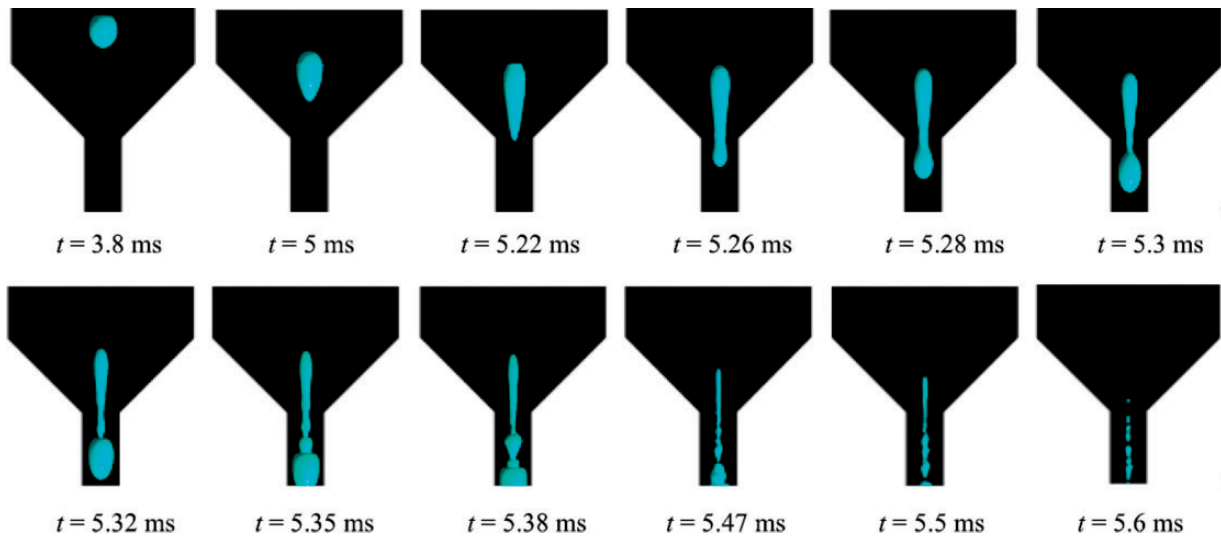


**Figure 18.** Shape of a single bubble passing through the exit orifice (case 7).

phase overflow occurs primarily in the beginning stage (5.32–5.47 ms).

Figure 19 shows the surface morphology of bubbles at two different times.

As Figure 19 shows, some bulges generate on the bubble surface in addition to the bubble expansion and tensile stretching. The two ends of each bulge are relatively slender, which is the primary cause to the rupture of the bubble, as shown in Figure 19(b). The complex flow field and surface tension distribution cause the wave-like morphology of the bubble.

Figure 19 also shows that the bubble inside the nozzle exit region is intensely stretched and even become elongated filaments. For bubbly flow, gaps between the bubbles could cause the flow discontinuity and jet instability. However, the bubble stretching occurs in the nozzle exit region could extend the distribution space of the gas phase, and thus the gaps between bubbles could be decreased, which would improve the continuity and stability of the jet.

Figure 20 shows changes in the volume, surface area, area-to-volume ratio, and tensile coefficient of the single bubble flowing through the nozzle exit region.

The bubble volume and surface area are divided by the initial bubble volume and surface area, respectively, to establish dimensionless parameters. The bubble area-to-volume ratio  $\theta_{SV}$  is defined as the ratio of the instantaneous bubble surface area to its volume. The tensile coefficient  $\varepsilon$  is defined by the ratio between the instantaneous bubble length and its initial length.

$$\text{Bubble area-to-volume ratio } \theta_{SV}: \quad \theta_{SV} = \frac{S_{\text{bubble}}}{V_{\text{bubble}}} \quad (21)$$

$$\text{Bubble tensile coefficient } \varepsilon: \quad \varepsilon = \frac{L_{\text{bubble}}(t > 0)}{L_{\text{bubble}}(t = 0)} \quad (22)$$

where  $S_{\text{bubble}}$  and  $V_{\text{bubble}}$  are the surface area and volume of single bubble in the nozzle exit region, respectively.  $L_{\text{bubble}}$  is the bubble length.

As Figure 20(a) shows, the developments of the dimensionless bubble volume and surface area with time are almost the same for the process of flowing through the nozzle exit region. Before the bubble entering the nozzle exit region ( $t < 5.2$  ms), the dimensionless

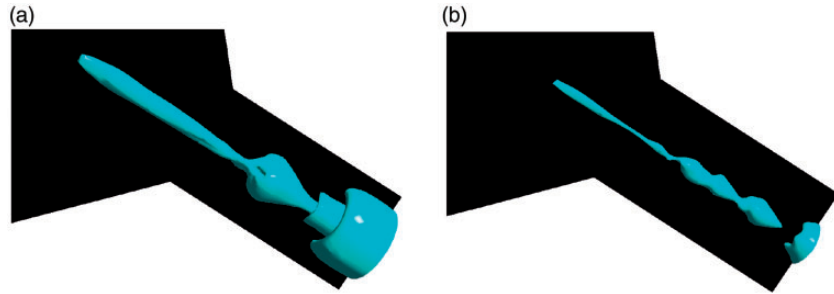


**Figure 19.** Surface shape of a single bubble in the exit orifice (case 7). (a)  $t = 5.38$  ms (b)  $t = 5.5$  ms.

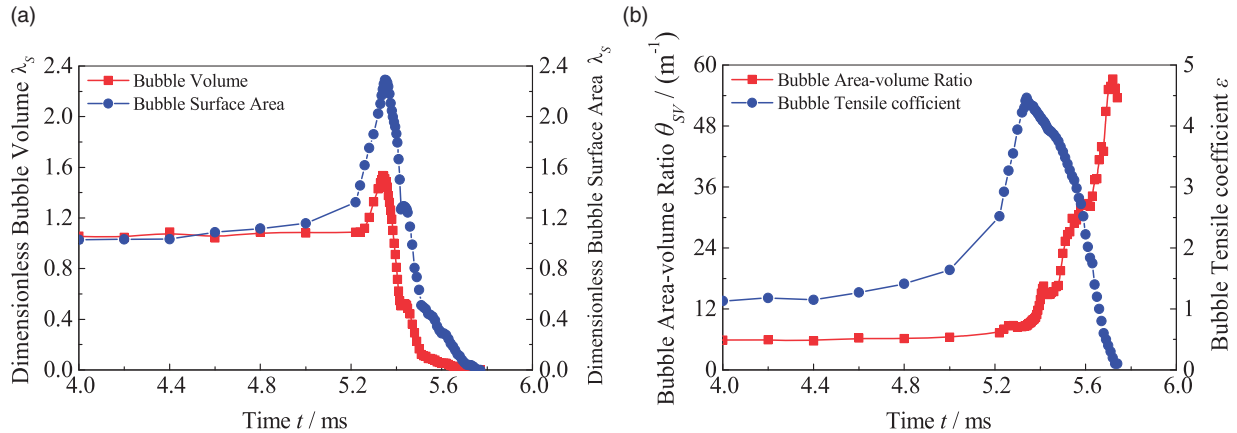


**Figure 20.** Variation in the shape parameters of a single bubble passing through the exit orifice (case 7). (a) Dimensionless bubble volume and surface area (b) Bubble area-to-volume ratio and tensile coefficient.



bubble volume is nearly constant, and the dimensionless surface area increases slightly because of the bubble deformation. As the bubble enters the exit orifice region and expands, the bubble dimensionless volume and surface area increase rapidly. The dimensionless bubble volume and surface area begin to decrease until the bubble overflows.

The bubble deforms slightly before entering the nozzle exit region ( $t < 5.2$  ms), which could be reflected by the bubble area-to-volume ratio, as shown in Figure 20(b). Both area-to-volume ratio and tensile coefficient increase rapidly since the bubble entering the nozzle exit region ( $t \geq 5.2$  ms), and the bubble shape changes from a sphere to a strip shape. The gas phase becomes increasingly slender during its passing through the nozzle exit region, and the bubble area-to-volume ratio will increase correspondingly.

Figure 21 shows the changes in the average bubble velocity and pressure over time for a single bubble passing through the nozzle exit region. It shows that the bubble velocity increases significantly and the bubble

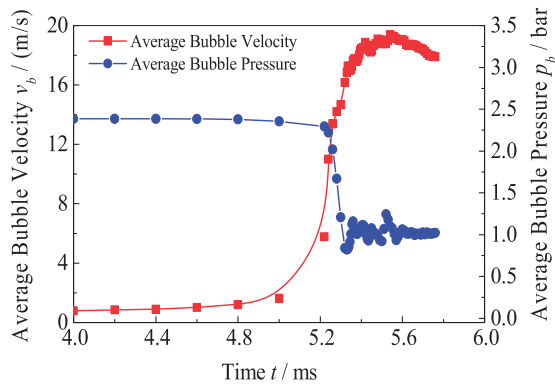


**Figure 21.** Variation in the flow parameters of a single bubble passing through the exit orifice (case 7).

pressure decreases rapidly in the nozzle exit region. There's a large difference in velocities between front and back of the bubble due to the pressure gradient, and it is the primary reason for the intense stretching of the bubble. After the bubble fully enters into the nozzle exit region, the bubble pressure begins to stabilize with a certain oscillation, and the bubble pressure may be even lower than the outlet pressure (1 bar). The bubble pressure oscillation and bubble morphology variation enhance the turbulent disturbance of the gas-liquid two-phase flow in the nozzle exit region.

The bubble's dramatic morphological change is closely related to the complex flow field inside the nozzle exit region. Figure 22 shows the flow field parameters (velocity and pressure) with the axial position at two different times. The instantaneous morphologies of the bubbles are also shown in Figure 22. The velocity and pressure at different axial positions are the mean values of the velocities and pressures in a longitudinal section of the current position.

As Figure 22 shows, the velocity and pressure in the nozzle exit region vary greatly with time. The fluctuation amplitude of the bubble morphology is proportional to the velocity fluctuation inside the nozzle exit region. This result shows, once again, that the flow morphology of the gas-liquid phase inside the nozzle exit region is significantly affected by the flow field.

The main physical mechanism of gas phase deformation inside the nozzle exit region such as bubble stretching and breakup is the competition of the surface tension and pressure difference force. Figure 23 gives the distributions of velocity and pressure on the bubble surface.

The bubble shape is closely corresponding to the distribution of velocity and pressure, as can be seen in Figure 23, and the local distributions of the bubble are very different. The distributions of velocity and pressure on the bubble surface show a non-monotone

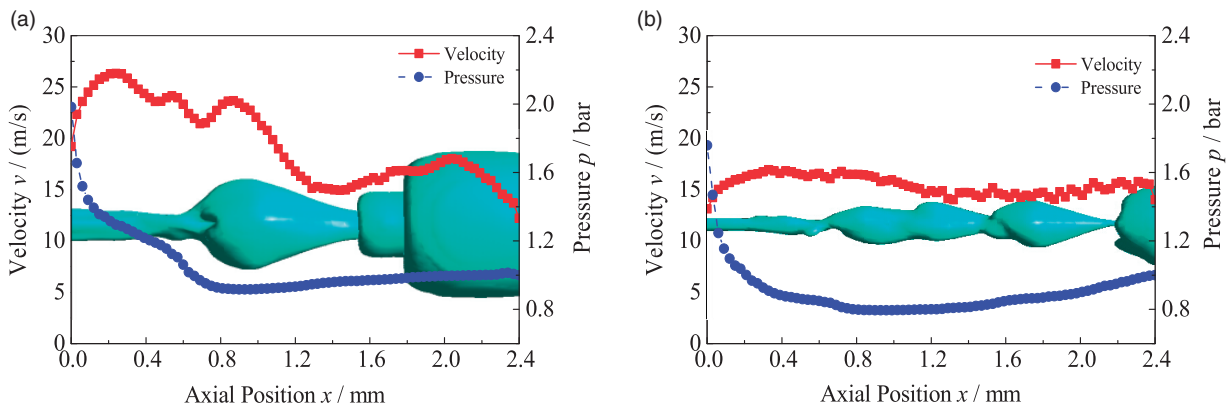


**Figure 22.** Velocity and pressure in the nozzle exit region (case 7). (a)  $t = 5.38$  ms (b)  $t = 5.5$  ms.

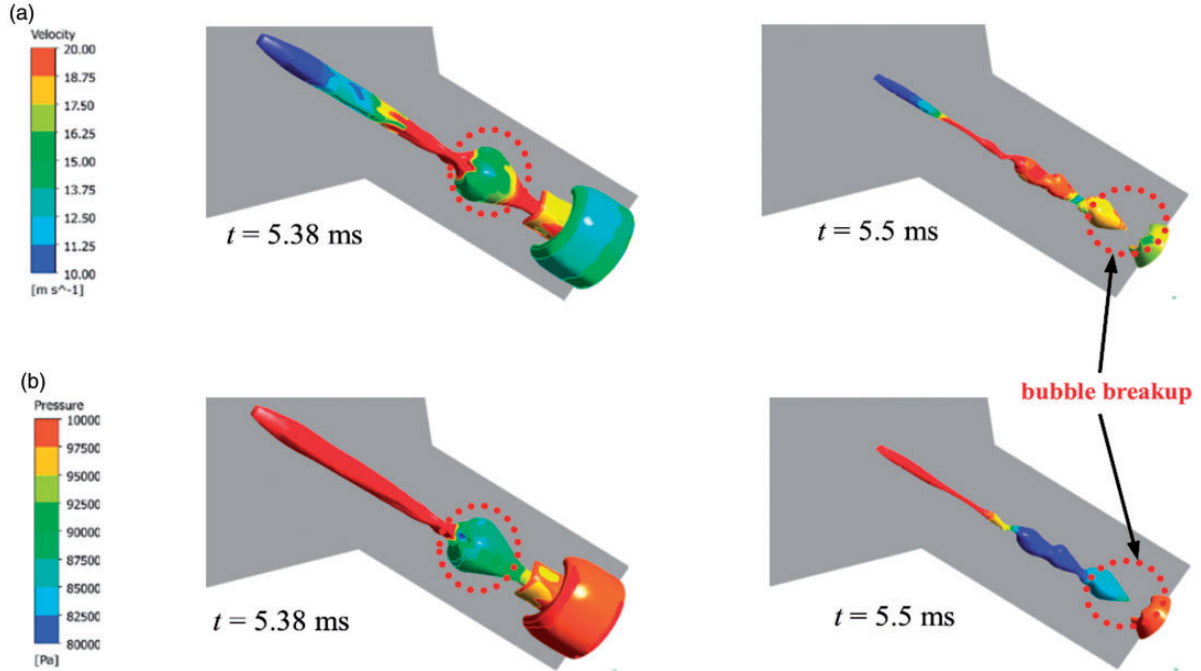


**Figure 23.** The (a) velocity and (b) pressure distribution on the bubble surface (case 7).

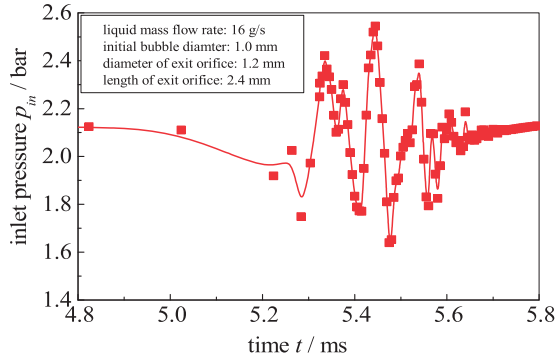


**Figure 24.** The inlet pressure of exit orifice versus time (case 7).

law along the axis. The force caused by pressure difference increases and overcomes the surface tension due to the local pressure drop on the bubble surface as marked in Figure 23(b).

There are mutual influences and interactions between the bubble deformation and the flow field around the bubble. The flow field change caused by the movement and deformation of the bubble not only reflects the disturbance of the bubble to the flow field, but also reflects the deformation characteristics of the bubble. Figure 24 shows the pressure at the inlet of the nozzle exit region.

It can be seen from Figure 24 that the pressure fluctuation at the inlet section of the nozzle exit region is severe since the bubble passing through the nozzle

( $t > 5.22$  ms). The pressure fluctuation attenuates since the “tadpole-shaped” bubble head passing through the nozzle ( $t > 5.4$  ms). The pressure fluctuation together with the pressure gradient leads to the rapid expansion of bubble, and the movement and expansion of bubble affect the flow field and give rise to fluctuation of liquid velocity in turn. Moreover, the Kelvin–Helmholtz (K–H) instability would occur in the gas–liquid interface in the nozzle exit region. The K–H wave formed in the atomizer will further affect the external flow and promote the liquid jet breakup. In addition, the expansion of gas will increase the gas void fraction, and subsequently affects the sound speed. The effect of gas expansion on the sound speed is quite different, according to the gas void fraction.<sup>28</sup> For low GLR and low gas void fraction, the increase of gas void fraction would decrease the sound speed. A lower sound speed means the flow might be choked, and it could hence the pressure jump at the exit which would cause bubbles to expand upon exiting the nozzle, which is beneficial for jet breakup.<sup>7</sup> While for high GLR low gas void fraction, the gas expansion could increase the sound speed, facilitating flow continuity and jet stability.

### 3.3. Characteristics of flow parameters at the exit section

The nozzle exit section is the outlet of the gas–liquid two-phase internal flow. The gas–liquid flow parameters at the exit section directly reflect the gas–liquid

mixing effect. Furthermore, the fluctuation characteristics of gas–liquid flow rate and gas void fraction are decisive parameters that affect the external spray performance.<sup>29</sup> Investigation of the fluctuation characteristics of the gas–liquid mass flow rate and gas void fraction at the exit section would contribute to understanding the spray characteristics.

Fluctuation of the flow parameters at the exit section is closely related to the gas–liquid flow regime inside the mixing chamber. Therefore, in this study, the flow parameters at the exit section of the effervescent atomizer are investigated under different flow regimes, as shown in Figures 25 to 27.

For effervescent atomization, the instantaneous gas–liquid mass flow rates and gas void fraction at the exit section have important effects on jet breakup and liquid droplet formation. Figure 25 shows the variation in gas–liquid mass flow rate and gas void fraction at the exit section with time under churn flow (liquid flow rate = 16 g/s, GLR = 1.2%).

As shown in Figure 25, for churn flow, the pulsation of the gas–liquid mass flow rate and gas void fraction was regular with time, and the change in pulse amplitude is relatively small. The small fluctuation of flow rates might be the reason for the stable spray under

churn flow as observed in the previous experiments.<sup>30,31</sup> The gas void fraction at the exit section increases significantly as a result of the gas expansion in the nozzle exit region. The gas void fraction is approximately 0.9, while the GLR is only 1.2%. The large gas void fraction contributes to smaller liquid filament formation and droplet breakup, and it makes the spray of effervescent atomization insensitive to the exit orifice diameter.

Figures 26 and 27 show the gas–liquid mass flow rate and gas void fraction at the exit section under discrete bubbly flow (liquid mass flow rate = 16 g/s, GLR = 0.07%) and slug flow (liquid mass flow rate = 8 g/s, GLR = 0.05%), respectively.

For bubbly flow, passage of a bubble through the nozzle exit region is a complex process which includes bubble expansion, deformation, and rupture. The complex gas–liquid two-phase flow behavior inside the nozzle exit region also affects the flow parameters at the exit section, as shown in Figure 26. Variations in the gas–liquid mass flow rate and gas void fraction with time show that the flow parameters at the exit section are relatively irregular compared to churn flow. The periodicity can be detected in the fluctuations of the flow parameters at the exit section. In each fluctuation cycle, the gas mass flow rate and gas void fraction

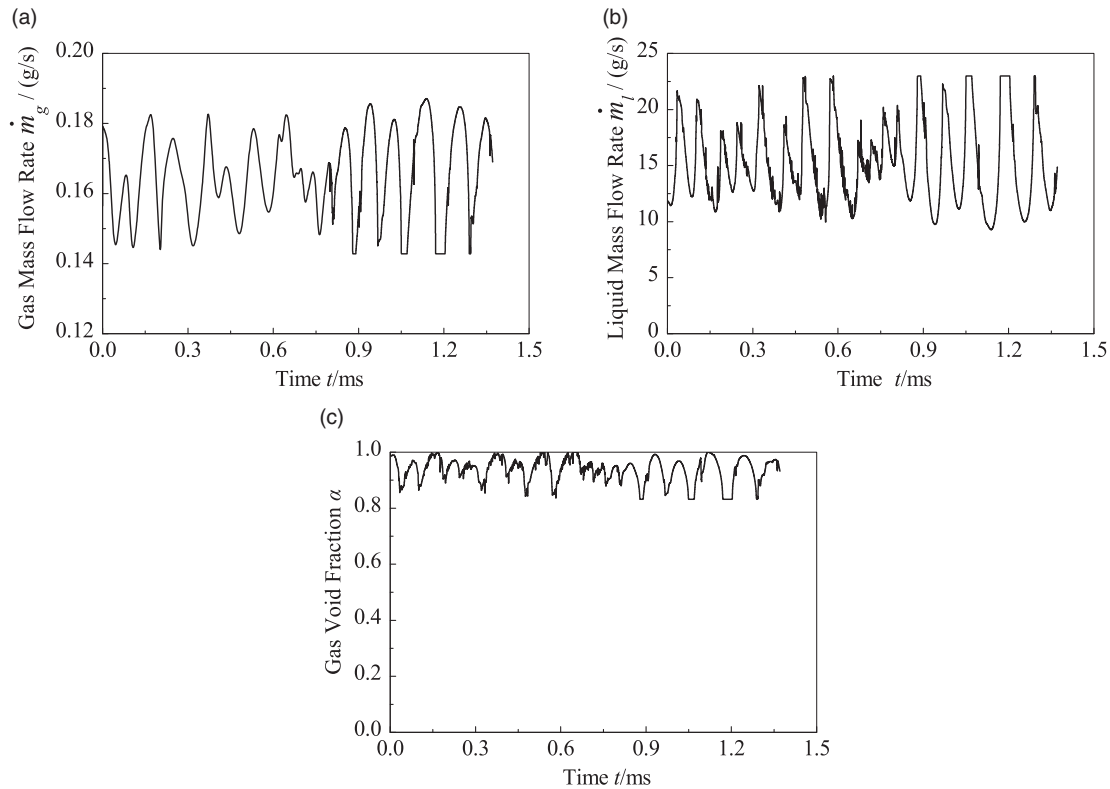


**Figure 25.** Variation in fluid parameters at the exit section under churn flow (case I). (a) Gas mass flow rate. (b) Liquid mass flow rate. (c) Gas void fraction.

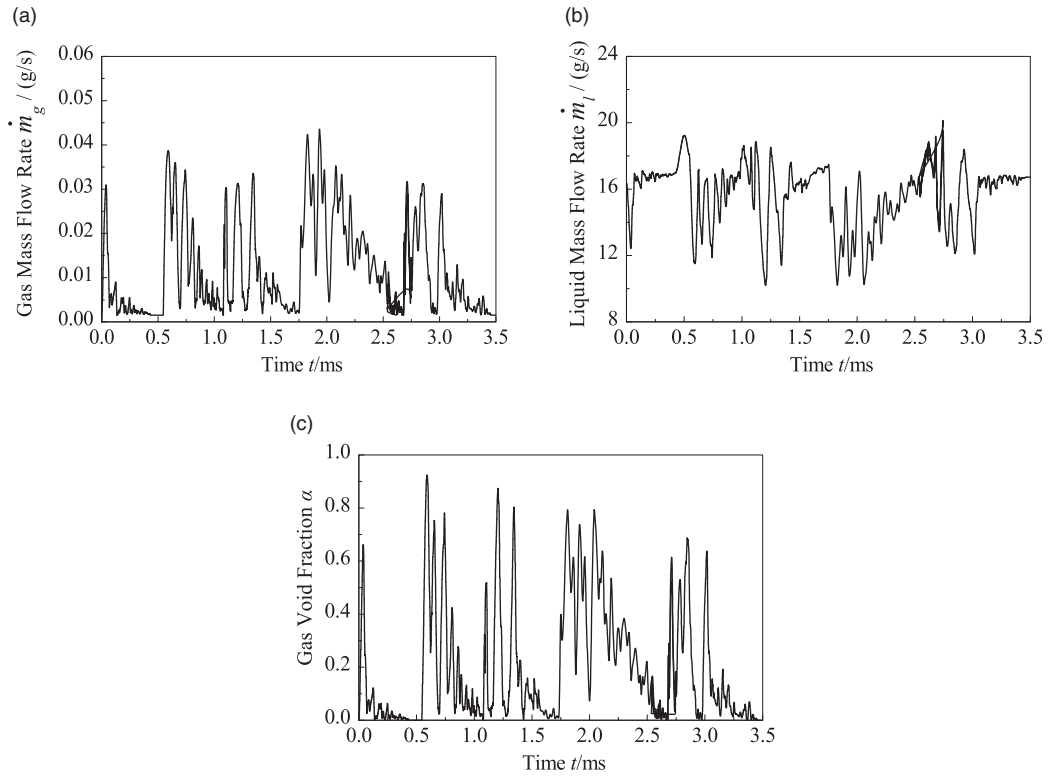


**Figure 26.** Variation in fluid parameters at the exit section under discrete bubbly flow (case 8). (a) Gas mass flow rate. (b) Liquid mass flow rate. (c) Gas void fraction.

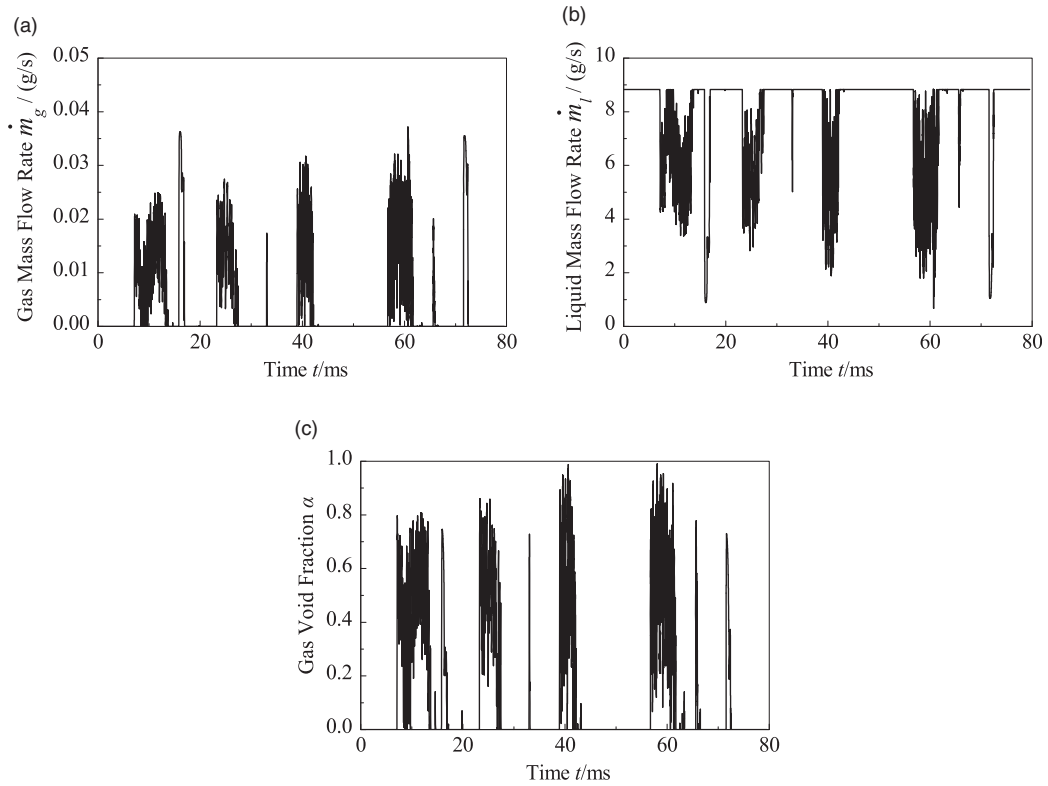


**Figure 27.** Variation in fluid parameters at the nozzle exit section under slug flow (case 6). (a) Gas mass flow rate. (b) Liquid mass flow rate. (c) Gas void fraction.

change with oscillatory decay form, which is likely due to the tadpole-shaped bubbles inside the nozzle exit region. Moreover, the fluctuation amplitude is larger than in churn flow.

Although the bubble stretching could effectively decrease the gap between bubbles and ease the discrete phenomenon to a certain extent, the pulsation in the flow parameters still has inevitable consequences for the spray continuity. For better spray performance, a larger number of bubbles with smaller size are desired, which is consistent with the results of Ghaemi et al.<sup>32</sup>

Figure 27 shows that the discrete distribution characteristics of the gas–liquid flow parameters are very obvious for slug flow. The gas void fraction reaches approximately 0.8 only when gas overflowing the nozzle exit, and the jet is in single liquid injection model for the rest of the time (gas void fraction is 0). This is extremely detrimental to the continuity of effervescent atomization.

#### 4. Conclusions

In effervescent atomizer, the gas–liquid two-phase flow behavior in the nozzle exit region is quite different from that in the mixing chamber. Study of the gas–liquid two-phase flow behavior in the nozzle exit region could deepen the understanding of the gas–liquid mixing process and is also an important basis for investigating the jet mechanism of effervescent atomizer. In this study, a numerical simulation method is used to investigate the gas–liquid two-phase flow in the nozzle exit region. Conclusions can be drawn as follows:

1. The flow behaviors inside the nozzle exit region under different upstream flow regimes differ significantly. For upstream churn flow, the liquid film morphology is closely related to the gas–liquid velocity fluctuation, and the liquid film will disappear at a low gas–liquid mass ratio. For upstream bubbly flow, differences in the gas volume and bubble shape have a direct impact on the instantaneous gas void fraction. In addition, multiple spherical bubbles will form a large “filamentous bubble” surrounded by liquid. For upstream slug flow, the morphological evolution of the gas slug is similar to that of a large single bubble in bubbly flow, and the average gas void fraction varies significantly with time.
2. The complex flow field and surface tension are the causes of wave-like morphology in bubbles. As a result of the effects of the pressure drop and surface tension, the bubble will form a tadpole-like shape. Tensile fracture will likely partially occur under the stretching action caused by the large pressure gradient. The bubble stretching in the nozzle exit region could extend the distribution space of the gas phase,

which could decrease the gap between bubbles and improve the continuity and stability of the jet.

3. The fluctuations in the flow parameters at the exit section under different upstream flow regimes also exhibit different characteristics. For churn flow, the pulsations of the gas–liquid mass flow rate and gas void fraction were regular with time, and the change in pulse amplitude is relatively small. The spray discontinuity could be restrained despite the larger consumption of gas. For bubbly flow, periodicity could be detected in the fluctuations of flow parameters at the exit section. In each fluctuation cycle, the changes in gas mass flow rate and gas void fraction are of oscillatory decay, and the fluctuation amplitude is larger than for churn flow, and it shows no interrupt of gas effect on jet by the adequate utilizing of the characteristic of gas expanding and stretching in the nozzle exit region. For slug flow, the gas phase occurs in the form of several gas slugs, and the discrete distribution characteristics of the gas–liquid flow parameters are very obvious, which is extremely detrimental to the continuity of effervescent atomization.

#### Declaration of Conflicting Interests

The author(s) declared no potential conflicts of interest with respect to the research, authorship, and/or publication of this article.

#### Funding

The author(s) disclosed receipt of the following financial support for the research, authorship, and/or publication of this article: Project supported by the National Natural Science Foundation of China (grant no. 51776016, 51606006, 91741122), Beijing Natural Science Foundation (grant no. 3172025, 3182030), China Postdoctoral Science Foundation (grant no. 2018M642014), Science Technology Department of Zhejiang Province (grant no. GG19E060001) and the National Engineering Laboratory for Mobile Source Emission Control Technology (grant no. NELMS2017A10).

#### ORCID iD

Chunhua Sun  <http://orcid.org/0000-0002-1266-7705>

#### References

1. Lefebvre AH, Wang XF and Martin CA. Spray characteristics of aerated-liquid pressure atomizers. *AIAA J Prop Power* 1988; 4: 293–298.
2. Lefebvre AH. A novel method of atomization with potential gas turbine application. *Indian Def Sci J* 1989; 38: 353–362.
3. Roesler TC and Lefebvre AH. Studies on aerated-liquid atomization. *Int J Turbo Jet Eng* 1989; 6: 221–230.
4. Kim JY and Lee SY. Dependence of spraying performance on the internal flow pattern in effervescent atomizers. *Atom Sprays* 2001; 11: 735–756.



5. Lin KC, Kennedy PJ and Jackson TA. Structures of internal flow and the corresponding spray for aerated-liquid injectors. In: *37th AIAA/ASME/SAE/ASEE joint propulsion conference*, Salt Lake City, UT, USA, 2001.
6. Ramamurthi K, Sarkar UK and Raghunandan BN. Performance characteristics of effervescent atomizer in different flow regimes. *Atom Sprays* 2009; 19: 41–56.
7. Shepard TG. *Bubble size effect on effervescent atomization*. PhD Thesis, University of Minnesota, Twin Cities, 2011.
8. Rahman MA. *Scaling of effervescent atomization and industrial two-phase flow*. PhD Thesis, University of Alberta, Edmonton, 2011.
9. Esfarjani SA and Dolatabadi A. A 3D simulation of two-phase flow in an effervescent atomizer for suspension plasma spray. *Surf Coat Technol* 2009; 203: 2074–2080.
10. Catlin CA and Swithenbank J. Physical processes influencing effervescent atomizer performance in the slug and annular flow regimes. *Atom Sprays* 2001; 11: 575–595.
11. Lörcher M, Schmidt F and Mewes D. Effervescent atomization of liquids. *Atom Sprays* 2005; 15: 145–168.
12. Li BR, Pan L and Yang G. Numerical studies of the flow structure in the final discharge orifice of effervescent atomizer. *Atom Sprays* 2012; 22: 259–274.
13. Lü M, Ning Z and Sun CH. Numerical simulation of cavitation bubble collapse within a droplet. *Comp Fluids* 2017; 152: 157–163.
14. Brackbill JU, Kothe DB and Zemach CA. A continuum method for modeling surface tension. *J Comput Phys* 1992; 100: 335–354.
15. Launder BE and Spalding DB. *Lectures in mathematical models of turbulence*. Pittsburgh: Academic Press, 1972.
16. Chin JS and Lefebvre AH. Design procedure for effervescent atomizers. *J Eng Gas Turbine Power* 1995; 117: 266–271.
17. Petersen FJ, Worts O, Schaefer T, et al. Design and atomization properties for an inside-out type effervescent atomizer. *Drug Develop Indus Phar* 2004; 30: 319–326.
18. Nielsen AF, Poul B, Kristensen HG, et al. Investigation and comparison of performance of effervescent and standard pneumatic atomizer intended for soluble aqueous coating. *Pharm Dev Technol* 2006; 11: 243–253.
19. Sun CH, Ning Z, Qiao XQ, et al. Measurements of internal flow regime and bubble size in effervescent atomizer. *Exp Therm Fluid Sci* 2018; 98: 604–620.
20. Mandhane JM, Gregory GA and Aziz K. A flow pattern map for gas–liquid flowing horizontal pipes. *Int J Multiphas Flow* 1974; 1: 537–553.
21. Liang XY. *Experimental research and numerical simulation on effervescent atomizer*. PhD Thesis, Southeast University, Nanjing, China, 2005.
22. Hewitt GF and Hall-Taylor NS. *Annular two-phase flow*. Oxford: Pergamon Press, 1970.
23. Brennen Christopher E. *Fundamentals of multiphase flow*. Cambridge: Cambridge University Press, 2009.
24. Sarkar UK and Ramamurthi K. Flow visualization of sprays formed by bubbly, slug, and annular flows in an effervescent atomizer. *J Flow Visual Image Process* 2007; 14: 397–408.
25. Sen D, Balzan MA, Nobes DS, et al. Bubble formation and flow instability in an effervescent atomizer. *J Visual* 2014; 17: 113–122.
26. Gadgil HP and Raghunandan B. Some features of spray breakup in effervescent atomizers. *Exp Fluids* 2011; 50: 329–338.
27. Santangelo PJ and Sojka PE. A holographic investigation of the near-nozzle structure of an effervescent atomizer-produced spray. *Atom Sprays* 1995; 5: 137–155.
28. Kieffer SW. Sound speed in liquid-gas mixtures: water-air and water-steam. *J Geophys Res* 1977; 82: 2895–2904.
29. Gomez J. *Influence of bubble size on an effervescent atomization*. Edmonton: University of Alberta, 2010.
30. Kleinhans A, Georgieva K, Wagner M, et al. On the characterization of spray unsteadiness and its influence on oil drop breakup during effervescent atomization. *Chem Eng Process Process Intens* 2016; 104: 212–218.
31. Hong M, Fleck BA and Nobes DS. Unsteadiness of the internal flow in an effervescent atomizer nozzle. *Exp Fluids* 2014; 55: 1–15.
32. Ghaemi S, Rahimi P and Nobes D. Effect of bubble generation characteristics on effervescent atomization at low gas–liquid ratio operation. *Atom Sprays* 2010; 20: 211–225.